

Tuning the Interlayer Distance of Graphene Oxide as a Function of the Oxidation Degree for *o*-Toluidine Removal

Eleonora Pargoletti, Marco Scavini, Saveria Santangelo, Giovanni Consolati, Giuseppina Cerrato, Martina Longoni, Salvatore Patané, Mariangela Longhi,* and Giuseppe Cappelletti


Graphene oxide (GO) with different oxidation degrees is prepared by a modified Hummers' method varying KMnO_4 amount from 0.5 to 6.0 g. X-ray powder diffraction (XRPD), micro-Raman, thermogravimetric analysis, X-ray photoelectron spectroscopy, Boehm titrations, high-resolution transmission electron microscopy, and, finally, positron annihilation lifetime spectroscopy (PALS) are exploited to assess the properties of GO. Results show that increasing oxidant species can tune the interlayer gap between GO sheets up to a maximum value in the case of 4.0 g KMnO_4 content. Moreover, these results validate the two-component-based model of GO in which, at low oxidation degree, there are unsplit/isolated graphene planes, instead at higher oxidant amounts, a five-layer sandwiched configuration occurs comprising graphene planes having functional groups decorating the edges (bwGO), hydrated oxidative debris (OD) and "empty" spaces (revealed by PALS as the distance between (bwGO + OD) two-component layers). In addition, by XRPD analysis, the total gap between two sheets is easily computed. In order to correlate these findings to pollutant removal capability, planar *o*-toluidine adsorption is studied. Since this molecule diffuses in an aqueous environment, the obtained adsorption percentages are compared to the thickness of the hydrated OD grafted onto bwGO. A strict connection between the pollutant removal efficacy and the variation of the hydrated interlayer distance is found.

1. Introduction

Since the discovery of graphene oxide (GO) in the 19th century, many researchers have focused their attention on exploring its remarkable potential for different applications.^[1–4] Indeed, this 2D material possesses very interesting electronic, thermal, optical, and mechanical features.^[5–7] In addition, its main advantage with respect to pristine graphene is the presence of an electronic band gap thanks to the oxygen-containing functionalities introduced by chemical treatment.^[8,9] Notably, the decoration of graphene sheets with oxygen groups also provides opportunities to tune the aforementioned properties by controlling the oxidation degree.^[1,10–13] However, the structure and chemical compositions of GO are still under debate since several hypotheses have been formulated up to now. According to the available literature,^[11,14,15] GO shows oxygen species mainly in the form of hydroxyl and epoxy groups, with a very small contribution of carbonyl and

E. Pargoletti^[†], M. Scavini, M. Longoni, M. Longhi, G. Cappelletti
Dipartimento di Chimica
Università degli Studi di Milano
via Golgi 19, Milano 20133, Italy
E-mail: mariangela.longhi@unimi.it

E. Pargoletti^[†], S. Santangelo, S. Patané, M. Longhi, G. Cappelletti
Consorzio Interuniversitario Nazionale per la Scienza e Tecnologia dei
Materiali (INSTM)
Via Giusti 9, Firenze 50121, Italy
S. Santangelo
Dipartimento di Ingegneria Civile
dell'Energia
dell'Ambiente e dei Materiali (DICEAM)
Università "Mediterranea"
Loc. Feo di Vito
Reggio Calabria 89122, Italy
G. Consolati
Department of Aerospace Science and Technology
Politecnico di Milano
via La Masa 34, Milano 20156, Italy

 The ORCID identification number(s) for the author(s) of this article can be found under <https://doi.org/10.1002/admi.202300179>

[†] Present address: The University of Sydney, Faculty of Engineering, School of Biomedical Engineering, Darlington 2008, Sydney, NSW Australia

© 2023 The Authors. Advanced Materials Interfaces published by Wiley-VCH GmbH. This is an open access article under the terms of the Creative Commons Attribution License, which permits use, distribution and reproduction in any medium, provided the original work is properly cited.

DOI: 10.1002/admi.202300179

carboxyl ones, which predominantly decorate the edges of the graphene sheets. Moreover, Johari et al.^[11] stated that all chemical formulas of GO, obtained experimentally, describe up to $\approx 75\%$ of graphene coverage as the combination of sp^2 and sp^3 carbon bonds. The sp^2 hybridization is related to the carbon atoms ascribable to both C=C bonds (between neighboring carbon atoms) and C bonded with oxygen in the form of carbonyl or carboxyl groups. Conversely, sp^3 hybridization is related to C–C and C–O bonds in epoxy and/or hydroxyl groups.

Therefore, the presence of these moieties guarantees the GO utilization in membranes and in the removal of non-biodegradable dyes, recalcitrant and emerging pollutants (such as methylene green,^[16] rhodamine B,^[17] tetracycline^[18] and bisphenol A^[4,19]) and heavy metals (e.g., Cd²⁺, Cu²⁺ or Pb²⁺^[20–22]). Actually, the high number of oxygen functionalities provides a low point-of-zero charge (pzc) and, at pH above 7, a strong negative surface charge for GO, activating the electrostatic interactions with the positively charged adsorbates. These interactions also comprise the hydrogen bonding between hydrogen atoms and highly electronegative atoms (such as oxygen, nitrogen, and fluorine) of the possible pollutant molecules. Furthermore, the sp^2 carbon bonds can give rise to π – π interactions with the benzene rings of the potential pollutants,^[23] and even create the cation– π bonding with metal ions/protonated amino groups.^[24] This unique capacity boosts the excellence of GO as a hot spot for the removal of contaminants in aqueous media.^[25,26] For instance, Xu et al.^[25] investigated aqueous toluidine blue removal by GO/bentonite composite material, resulting in a significant improvement of the adsorption capacities of the natural clay, thus paving the way for the design of promising advanced adsorbents. Parallely, GO-based membranes have been recently reported to exhibit prominent permeation properties toward gases, liquids, and vapors.^[27,28] For example, micrometric-thick membranes have been demonstrated to be selective and highly permeable to water molecules.^[2,29] Indeed, owing to the unique GO atomic-thin nanosheets assembled into 2D-nanochannels, graphene oxide-based membranes can be very successful for the precise ionic and/or molecular sieving of aqueous solutions.^[30]

In both the previous applications, the final behavior can be tailored by varying the oxidation degree and, hence, the interlayer distance between GO sheets plays a fundamental role. Several authors already investigated the different oxidation degrees of graphene oxide.^[31,32] They evidenced the correlation between this parameter and the GO intrinsic electrochemical properties,^[32] its optical features, and the electrical resistance^[31] but without a direct application, as for molecules intercalation, electrocatalysis, etc. Moreover, Sakthivel et al.^[10] gave an insight into the assessment of the GO interlayer distance with the increase of the oxidation degree i.e., by increasing the amount of oxidizing agent

in the synthetic route. They found that GO prepared by using the greatest amount of potassium permanganate in the modified Hummers' method (namely 8.0 g) leads to almost complete removal of aqueous methylene blue. Nevertheless, so far, a possible relationship between the GO interlayer distance and the material adsorption capacity has not been discussed yet.

Herein, we report a deep analysis of the modification of the GO properties by increasing the oxidation degree, focusing on the interlayer gap by means of several physicochemical techniques, including the innovative positron annihilation lifetime spectroscopy (PALS). Finally, to the authors' best knowledge, a correlation between the peculiar GO features and the materials' adsorption capacity toward *o*-toluidine, chosen as a representative molecule among harmful aqueous pollutants, is discussed for the first time. Actually, this aromatic amine is known to possess carcinogenic properties for animals and humans, even at low concentrations, and it is present in the environment due to its large use, for example, as precursors of azo-dyes, in the rubber industry and pharmaceutical productions.^[33,34] Therefore, the fabrication of an efficient adsorbent/intercalating material is one of the current issues to be solved and is of crucial importance for both environmental and healthy perspectives.

2. Results and Discussion

2.1. Structural, Morphological, and Surface Properties of Differently Oxidized GO

With the purpose to unveil the role played by potassium permanganate as an oxidizing agent in the Hummers' method, the synthesized powders were finely investigated from different physicochemical points of view.

Figure 1a shows the relative X-ray powder diffraction (XRPD) patterns with evidence of the main Bragg's peaks together with the corresponding Miller's indexes. The pattern of the GO_0.5 sample displays a large bump centered at $2\theta \approx 16.4^\circ$, with a very small peak at a smaller angle (at $\approx 11.5^\circ$, Figure 1b). These can be ascribable to the incipient formation of a GO phase^[40]; the very tiny peak labeled with a star could indicate the insertion of water in a few GO zones.^[39] It is followed by a reasonably sharp (002)_{GR} reflection at $2\theta \approx 26.3^\circ$ that dominates the patterns, highlighting that graphite is the principal crystalline phase in this sample. The presence of (100)_{GR} and (110)_{GR} peaks in the 42 – 44° 2θ range evidences the good crystallinity of the graphite phase (Figure S1, Supporting Information). Moving to GO_2.0 powder, the (002)_{GR} peak disappears, whereas the (001)_{GO} reflection shifts to smaller angles ($2\theta \approx 12.5^\circ$), sharpens and enlarges its intensity, thus dominating the XRPD pattern. This asymmetric peak may indicate that GO accommodates water molecules not uniformly with a larger amount of more hydrated planes. Indeed, the peak at $\approx 12.5^\circ$ dominates and the other one is a simple shoulder (see Figure 1b). In the patterns of samples GO_4.0 and GO_5.0, the reflection (001)_{GO} remains asymmetric, but it moves gradually to slightly smaller 2θ angles and asymmetry tends to decrease until it disappears in GO_6.0. This fact highlights how an increased amount of KMnO₄ could induce a raise of water amount in GO reaching a maximum in GO_6.0, while the shift of the peak maximum might be due to a slight increment of basal spacing.^[39] Concomitantly, the (002)_{GR} gets smaller and disappears.

G. Cerrato
Dipartimento di Chimica & NIS
Università degli Studi di Torino
Via P. Giuria 7, Torino 10125, Italy

S. Patané
Dipartimento di Scienze Matematiche e Informatiche
Scienze Fisiche e Scienze della Terra (MIFT)
Università di Messina
Viale Stagno d'Alcontres 31, Messina 98166, Italy

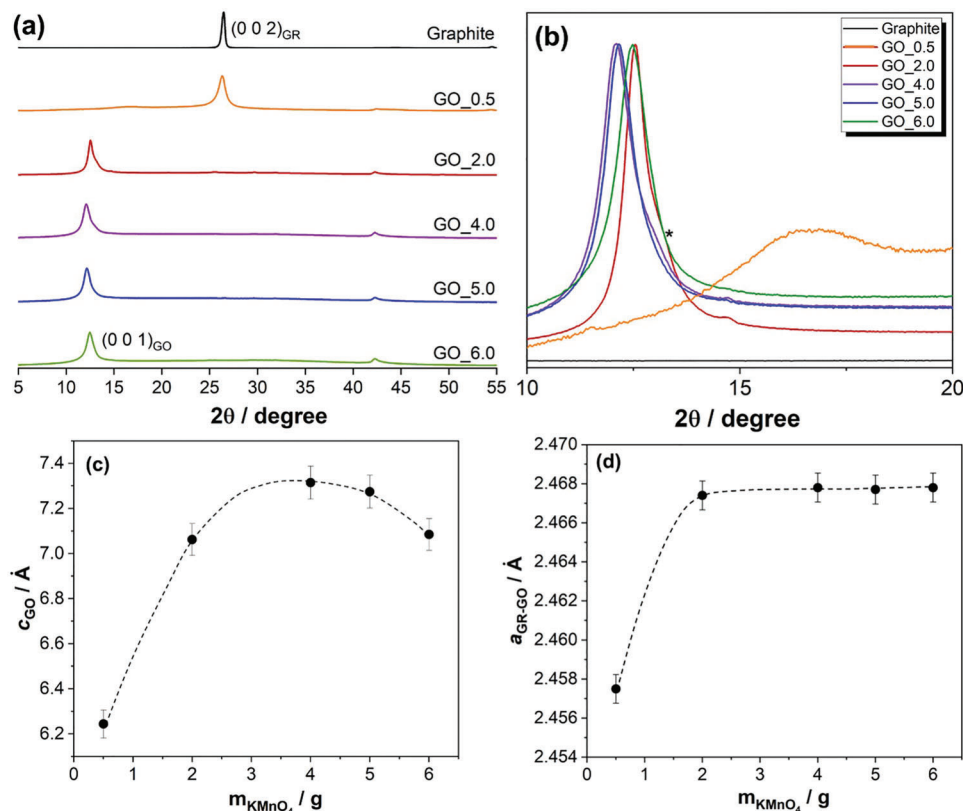


Figure 1. a) Comparison of XRPD spectra relative to graphite and all the synthesized GO powders. b) Focus on 10–20° 2θ range. c) c - and d) a -axis values trend with the increase of the oxidation degree (i.e., KMnO_4 amount increment).

Interestingly, the trend of the (001)_{GO} peak position on increasing the KMnO_4 amount is inverted in the GO_{6.0} sample. However, this apparent incongruence is justified considering that in this case there is only one peak and not a peaks combination as in the other samples. By using the hexagonal structure of graphite, as a reference, c and a -axes of the different GO were plotted and reported in Figure 1c,d. In particular, the c -axis corresponds to the interlayer distance between two consecutive graphene planes. Being asymmetric, the (001)_{GO} peak was fitted adopting two pseudo-Voigt functions and the most intense peak was considered to compute c -axis values (Figure 1c). Notably, passing from GO_{0.5} to GO_{4.0}, the interlayer distance increases until a maximum and slightly decreases for sample GO_{6.0}. Figure 1d, instead, exhibits the trend of the a -axis. Particularly, in GO_{0.5} the value of 2.458 Å reflects the graphite-like nature of this sample, whereas in GO_{2.0} it expands (≈ 2.468 Å) remaining almost the same in all the other powders. Moreover, the increase of the a -axis reflects the expansion of the in-plane C–C distance $d(\text{C–C})_{\text{ip}}$ with the increase of the amount of the oxidizing agent: in GO_{0.5} the $d(\text{C–C})_{\text{ip}}$ is ≈ 1.419 Å as in pure graphite, whereas in the other GO samples, the calculated $d(\text{C–C})_{\text{ip}}$ is 1.425 Å. This small bond expansion may be considered an indirect probe of the partial loss of aromaticity in the graphite-like planes of GO because of the greater oxidation degree. It is noteworthy to highlight that oxidation should push C hybridization toward some sp^3 character, thus causing the buckling of the graphene

planes. In this case, the actual increase of C–C interatomic distances should be even larger than our rough estimation.

To corroborate these observations, micro-Raman, thermo-gravimetric (TGA), and x-ray photoelectron spectroscopy (XPS) analyses were performed. Figure 2 displays the results of the micro-Raman analysis. The spectrum of GO_{0.5} is very different from that of crystalline graphite and closely reminds that of defective one (Figure 2a). The spectrum of crystalline graphite is dominated by a narrow band at 1582 cm^{-1} (G-band) and by a composite band centered at $\approx 2700\text{ cm}^{-1}$ (G'-band). The former, commonly regarded as the Raman fingerprint of the graphitic crystalline arrangement, arises from the E_{2g} symmetry stretching mode of all sp^2 bonded C=C pairs.^[45] Instead, the latter, sensitive to the stacking order,^[46] results from the superposition of two components that reflect the splitting in the π -electrons dispersion caused by the strong interaction between the basal planes. A very weak band at 1346 cm^{-1} (D-band) is further detected due to finite size effects that break the basic translational graphene-sheet symmetry and relax the selection rules.^[45] In defective graphite, all bands broaden due to the increase of structural disorder and the D-band intensifies strongly. As the 3D ordering in the lattice is partially lost, a third component, associated with the long-range 2D ordering, begins to contribute to the G'-band intensity, indicating the co-existence of 2D and 3D graphitically ordered phases.^[46,47] In nanocarbons with solely 2D ordering, characterized by weaker basal plane interaction, only the latter component

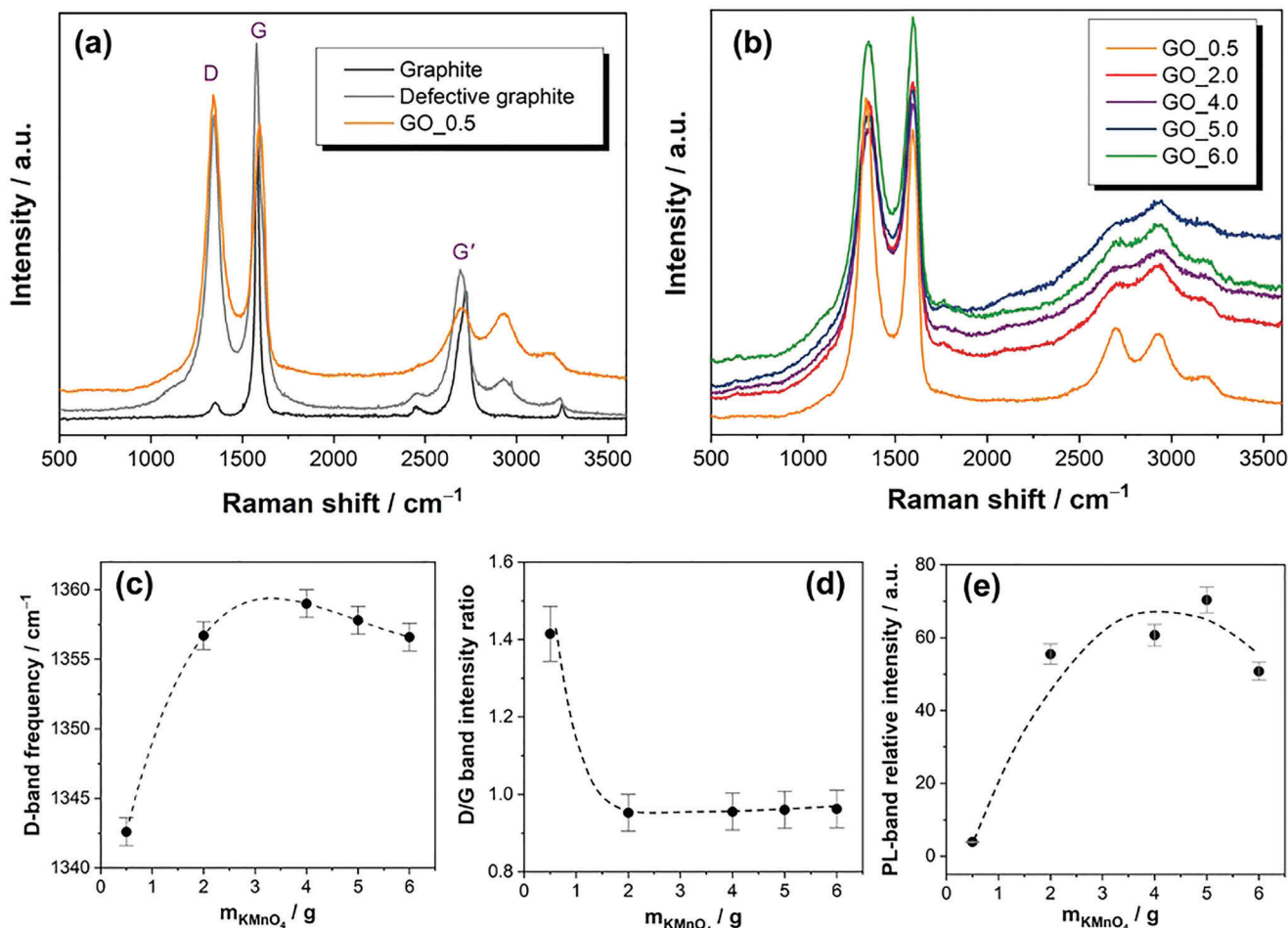


Figure 2. Results of micro-Raman analysis. a) Spectrum of sample GO_{0.5} compared with those of highly crystalline and defective graphite. b) Spectral evolution caused by the increase of KMnO₄. c–e) Main parameters inferred from the spectra fitting as a function of the KMnO₄ amount: c) D-band frequency position, d) D/G band intensity ratio, and e) PL-band relative intensity.

contributes to the intensity of the G'-band.^[46,47] The lower frequency region of the spectrum of GO_{0.5} is featured by a very intense D-band; in the higher frequency region, in addition to the G'-band (also known as 2D-band as it is ascribed to the overtone of the D-band^[47]), two broad bands are detected at 2940 and 3170 cm^{-1} . The latter, known as the 2G-band, is attributed to the overtone of the G-band, while the former is a combination ((D + G) band).^[42] Figure 2b shows the spectral evolution caused by the increase of KMnO₄. Compared to the spectrum of GO_{0.5}, all bands in the spectra of the remaining samples appear broadened and the intensity of the D and 2D bands is weaker. Besides, starting from sample GO_{2.0}, a photoluminescence (PL) background appears and progressively intensifies with the increase of potassium permanganate up to 5.0 g; then, it slightly weakens.

In order to infer additional information on the sample microstructure, the spectra were quantitatively analyzed by following literature references.^[42] Gaussian bands were used to reproduce the spectra (Figure S2a, Supporting Information). The main results obtained are shown in Figure 2c–e. The D-band significantly upshifts moving from sample GO_{0.5} to

GO_{2.0} (Figure 2c). The frequency position of the band further increases with the increase of the oxidizing agent amount up to 4.0 g, then it starts to decrease, showing a trend similar to that of the interlayer distance c (Figure 1b). The upshift of the D-band is commonly understood as the effect of the electron transfer from the π states in the carbon network to the oxygen atoms introduced by the oxidizing agent.^[48] The band moves toward higher frequency with the increasing of the oxidation degree, which explains the similarity with the changes in the c -axis produced by the accommodation of oxygenated species between the graphite-like planes of GO.^[49] The relative intensity of the D-band undergoes a drastic decrease moving from sample GO_{0.5} to GO_{2.0} (Figure 2d). Any further increase in potassium permanganate causes no other variations. The trend is analogous to the one observed for the lattice parameter related to the in-plane C–C distance (Figure 1c), which is not surprising as the disorder-activated band is associated to the A_{1g} symmetry in-plane breathing mode of the C hexagonal rings.^[45] Since only the sp^2 defects contribute to the D-band intensity,^[45] its decrease is understood as due to the increase in non- sp^2 defects,^[50] in line with the partial loss of aromaticity in the graphene planes of

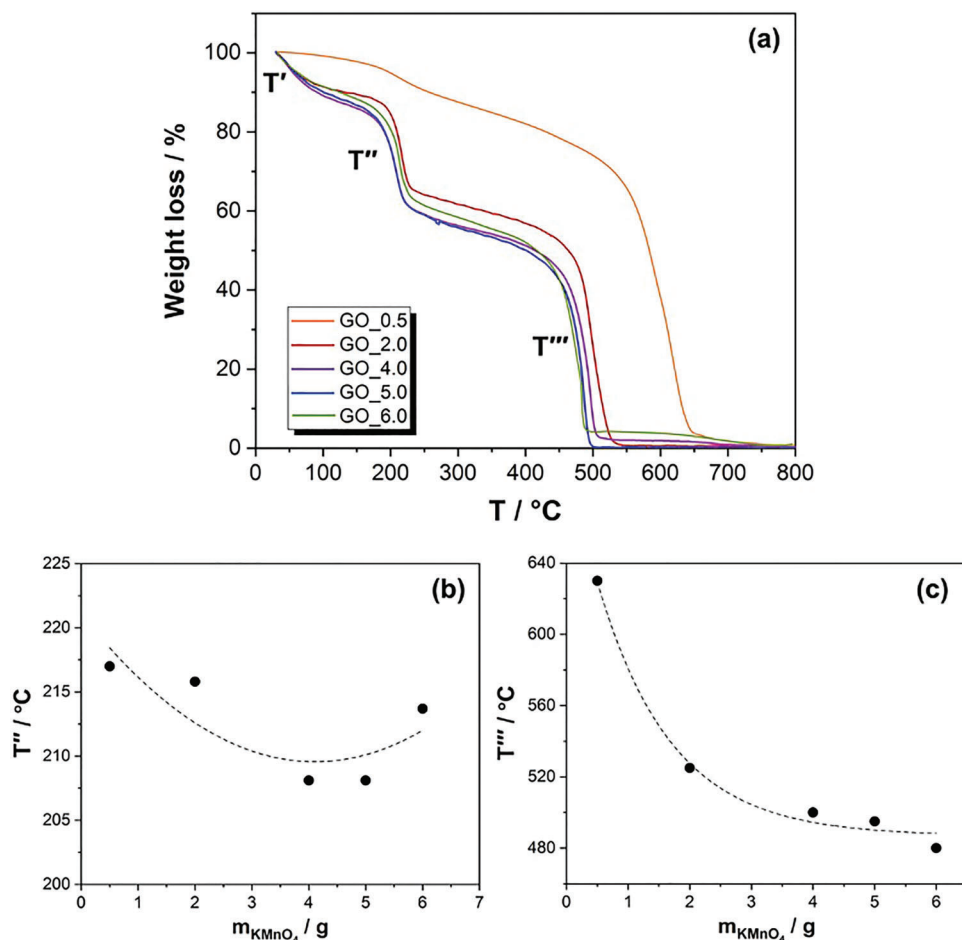


Figure 3. a) Thermogravimetric curves. Maximum temperatures of the TGA first derivatives are relative to the weight loss in the ranges b) $\approx 200\text{--}250\text{ }^{\circ}\text{C}$ (T') and c) $\approx 400\text{--}600\text{ }^{\circ}\text{C}$ (T'''), with the increase of the oxidation degree (i.e., KMnO_4 amount increment).

GO as a consequence of the greater oxidation degree, previously inferred by XRPD analyses. In sample GO_2.0, a PL band appears centered at $\approx 1.88\text{ eV}$ (660 nm, Figure S2b, Supporting Information). The band progressively intensifies as the amount of oxidant increases up to 5.0 g and then its intensity decreases slightly (Figure 2d). As a zero-bandgap material, pure graphene does not exhibit PL. As it is oxidized to form GO, its structure is distorted and a sp^3 component is introduced in the C bonding. The consequent disruption of the π -electron network of the carbon atoms opens a gap between the valence and the conduction bands and introduces a broad distribution of disorder-states with lower energy than the $\pi\text{--}\pi^*$ gap. These disorder-induced states are responsible for the broad PL band in the visible range (long wavelength or LW band).^[51] Then, if GO is reduced, both the sp^3 C bonding component and the number of disorder states decrease, while confined sp^2 C clusters form having higher energy than the disorder states. As a result, a new PL band appears at a lower wavelength.^[50,51] Here, the increase of the PL-band intensity reflects the increase in the number of disorder-states and, thus, indirectly monitors the increase in the oxidation degree obtained by increasing the quantity of KMnO_4 adopted to produce GO by the modified Hummers' method. The small intensity decrease observed in sample GO_6.0 might be due to the detachment of

oxidative debris (OD)^[50] in the presence of a higher disruption level of the pristine carbon network, resulting in an apparently lower oxidation degree. Indeed, a linear correlation (Figure S2c, Supporting Information, $R^2 = 0.974$) is found between the relative intensity of the PL band at 1.88 eV and the interlayer "empty" distance measured by the PALS technique (see below).

Thermogravimetric analysis data, displayed in **Figure 3a**, reveal the typical behavior of graphene oxide powder. Indeed, three main weight losses are appreciable: *i*) the first one (T') due to water loss (between 60 and 110 $^{\circ}\text{C}$)^[52]; *ii*) the second one (T'') showing a $\approx 20\%$ loss at $\approx 200\text{ }^{\circ}\text{C}$, which corresponds to the decomposition of the labile oxygen-containing groups with the generation of CO , CO_2 , and water^[53]; and *iii*) the most intense one (T'''), at $\approx 480\text{ }^{\circ}\text{C}$, caused by the π carbon bonds breaking in the hexagonal structure, thus indicating its thermal decomposition.^[52] TGA curves are very similar to each other except for that of GO_0.5, which displays the smallest weight loss in the first region, in accordance with XRPD data showing that GO_0.5 accommodates few water molecules, and an uncertain weight loss of $\approx 5\%$ in the second region (T''). Conversely, the other samples exhibit in T'' region a well-defined weight loss, of $\approx 23\text{--}24\%$ without a real dependence on the amount of permanganate used in the synthesis. This variation underlines that oxygen functionalities content

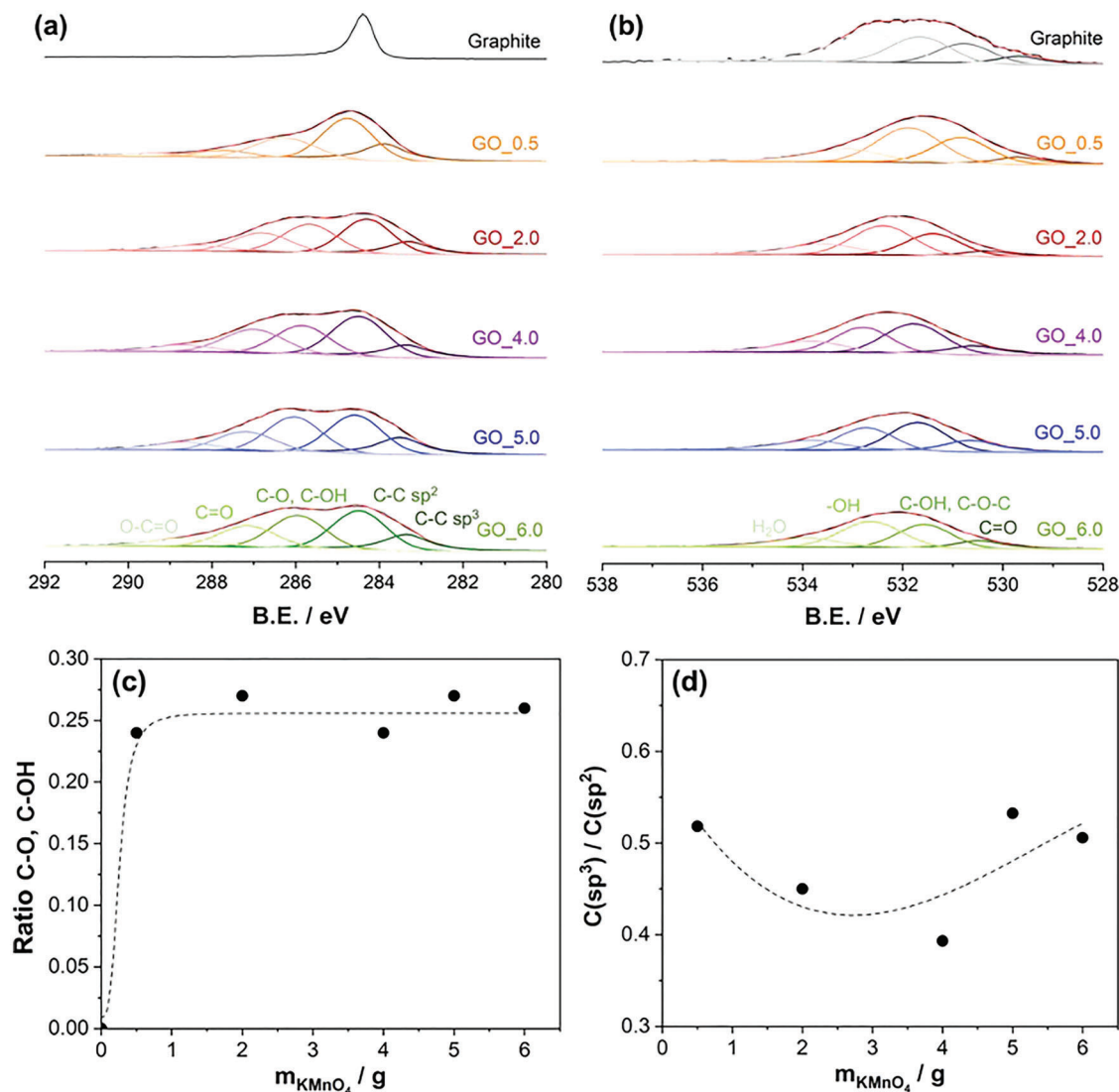


Figure 4. Core level high-resolution spectra relative to a) C1s and b) O1s regions. c) C–O, C–OH-peak, and d) C(sp^3)/C(sp^2) ratios (between counts of each peak and the total counts, from the deconvolution of the C1s region) with the increase of the oxidation degree.

increases from GO_0.5 to GO_4 till the achievement of a sort of plateau for GO_5 and GO_6. The third region shows similar weight losses for all samples ($\approx 50\%$) apart from GO_0.5 one ($\approx 80\%$). This difference is ascribable to the fact that GO_0.5 is much more similar to the starting graphite and the structural interactions are quite different from those of the other samples. By computing the first derivative of the curves in correspondence with the two major losses, that is, at ≈ 200 (T'') and 480 (T''') $^\circ\text{C}$, two interesting behaviors can be noticed that confirm the previously reported outcomes. Figure 3b shows the second loss temperature trend with respect to the amount of KMnO_4 used. Notably, by increasing the GO oxidation degree, the temperature at which oxygen-containing groups are decomposed decreases (by ≈ 10 degrees), reaching a sort of minimum for GO_4.0 and GO_5.0 and increasing again in GO_6.0, roughly replicating the trend observed by analyzing the micro-Raman spectra (Figure 2c). Figure 3c evidences that the temperature related to π

carbon bonds breaking gradually reduces passing from GO_0.5 ($\approx 630^\circ$) to GO_6.0 ($\approx 480^\circ$): this behavior is consistent with the higher reactivity of GO samples with decreased sp^2 hybridization in favor of non- sp^2 one^[50,53] (as signaled by the decrease of the relative intensity of the D-band).

In addition, even XPS and Boehm titrations support previous observations. High-resolution spectra with the relative deconvolution peaks of both carbon (C 1s) and oxygen (O 1s) regions are reported in Figure 4a,b, together with the corresponding data in Table S1 (Supporting Information). As far as it concerns the C 1s core level high-resolution spectra of the different GO samples (Figure 4a, Table S1, Supporting Information), five components are ascribable to the carbon atoms in different functional groups. In particular, the C–C sp^3 band appears at ≈ 283.5 eV, the C–C sp^2 at ≈ 284.4 eV, the C in C–O, C–OH bonds at ≈ 286.0 eV, the carbonyl C=O, epoxies, quinones, and lactones combined with lactol at graphene edges at 287.0 eV and the carboxylate carbon O=C–O

Table 1. Average basic functional group concentrations for all the synthesized GO powders determined by Boehm titrations on three replicates. Specific surface area (S_{BET}) and total pores volume ($V_{\text{tot. pores}}$) by BET-BJH analysis.

Sample	$c_{\text{basic groups}} / [\mu\text{eq g}^{-1}]$	$S_{\text{BET}} / [\text{m}^2 \text{g}^{-1}]$	$V_{\text{tot. pores}} / [\text{cm}^3 \text{g}^{-1}]$
GO_0.5	600 ± 100	10	0.030
GO_2.0	600 ± 200	7	0.013
GO_4.0	320 ± 20	22	0.021
GO_5.0	170 ± 80	24	0.020
GO_6.0	300 ± 100	16	0.023

at 288.7 eV.^[5,54] Only graphite exhibits a single peak at 284.4 eV relative to C–C sp^2 bonds. Similarly, the O 1s region (Figure 4b, Table S1, Supporting Information) consists of four different components relative to C=O (at 529.7 eV), O–C–O (at 531.5 eV), –OH (at 532.5 eV) and chemisorbed H_2O molecules (at 533.5 eV).^[55,56] Figure 4c,d displays the percentage of C–O, C–OH bonds (considering the C 1s region) with the increasing KMnO_4 amount, as well as the variation of the ratio between C sp^3 and C sp^2 .^[57] In the former case, a rise till the plateau is clearly observable, especially for GO_4.0, GO_5.0, and GO_6.0, corroborating once again a higher and comparable oxidation degree for these samples. Instead, by analyzing $C(sp^3)/C(sp^2)$ ratios, a minimum can be noticed for GO_4.0 powder followed by a further increment for the higher oxidated graphene oxides. As such, GO_5.0 and GO_6.0 seem to have a greater content of oxygen-containing functionalities – this is in accordance with the total oxygen percentage obtained from the survey: 29.2% and 28.1%, respectively – to the detriment of C sp^2 bonds.

An analogous discussion can be done by analyzing Boehm titration data (Table 1, second column). This method, developed for active carbon, relies on the principle that oxygen groups on carbon surfaces have different acidities and, therefore, can be neutralized using bases of different strengths. Specifically, the strongest one (NaOH) was used to titrate all Brønsted acids (including phenols, lactic groups, and carboxylic acids), sodium carbonate to neutralize carboxylic and lactic groups and, finally, sodium bicarbonate to determine carboxylic acids. Therefore, the difference between the uptake of two bases can be used to identify and quantify the types of oxygen-containing groups present on the carbon surfaces. Conversely, to determine the concentration of basic groups, hydrochloric acid was adopted. Despite the simplicity of the procedure, the acidic groups' determination experienced several issues. In some cases, the number of acidic groups with intermediate pK_a (typically lactone-like functions) obtained by subtraction according to the Boehm method,^[43] was less than zero thus giving a non-sense result. This outcome seems to suggest that samples in sodium bicarbonate have more acidic groups than in carbonate, and therefore there is an overestimation of acidic functions with small pK_a (i.e., carboxylic-like groups).

An attempt to rationalize this behavior starts by considering the existence of different models that describe the structure of GO. Indeed, in addition to the well-established one based on considering GO as a one-component material in which there is a coexistence of carbon sp^2 islands and sp^3 carbon region featur-

ing oxygen-containing functionalities,^[58] a more complex model based on a two-component description has been proposed^[59]: the first one is graphene with low oxidation degree showing functional groups decorating the edges of its plane (bwGO), insoluble at any pH, whereas the second one is oxidative debris (OD), composed of humic-like substances (insoluble at pH greater than 2) and fulvic-like fragments (soluble at any pH).^[60] This debris strongly adheres to the graphene plane by means of π – π stacking and hydrogen bonds.^[59] The presence of these two components can be seen in the high-resolution transmission electron microscope (HR-TEM) images of our more oxidized sample (Figure 5e; Figure S3b, Supporting Information): notably, graphene planes are combined with “messy” sheets with some apparent dots (OD),^[60] barely appreciable in GO_0.5 sample (Figure S3a, Supporting Information). Furthermore, this model sheds new light on TGA results since, in this case, the T'' region could be attributable both to the decomposition of the labile oxygen-containing groups and to the conversion in CO, CO_2 , and H_2O of OD and T''' to the decomposition of bwGO.^[60,61] While in GO_0.5 the relative percentage of OD is $\approx 6\%$, confirming its scarce presence in this material, in the other samples GO is composed of $\approx 32\%$ OD and $\approx 70\%$ bwGO, in accordance with literature data.^[60,61] Furthermore, these two components can be easily separated by means of alkaline treatment, since the increase of pH increases the negative charge on the deprotonated debris repelling them from the graphene planes.^[59] Therefore, this stripping process needs an alkaline solution to occur, albeit a pH ≈ 7 is sufficient to induce an OD leaking, in a longer time (more than 20 h).^[61] Finally, OD in solution tends to aggregate: at higher pH, a lower aggregation tendency occurs; whereas, at lower pH (≈ 2) this tendency increases.^[61] Herein, in the first 24 h equilibration step of Boehm titrations, OD is released in the solutions of NaHCO_3 , Na_2CO_3 , and NaOH. Since the released OD amount does not depend on the strength of the adopted bases, it can be supposed that the OD total amount is the same for the three alkalis. However, due to different pH, OD can aggregate in a different way: particularly, the most aggregated system should be in the presence of sodium bicarbonate, whereas the most separated one in NaOH. Alkaline solutions neutralize acidic groups on both the graphene planes edge and OD exposed to the solution, so the neutralized functions amount does not only depend on the base strength but also on the aggregation of OD, since with a higher aggregation degree much more groups are “hidden” by intimately linked neighborhood debris. After centrifugation, OD remains in the solution and, when hydrochloric acid is added to perform the back titration, its acidic functional groups are protonated, and it aggregates. Furthermore, statistically, the probability of aggregation in the same way in the three different solutions is close to zero, even considering that ionic strength, therefore the surface charge, is different. Hence, the three systems are different, but after adding HCl, exposed acidic functional groups of OD are also titrated causing an increased number of acidic functionalities due to OD disaggregation. Specifically, depending on the ionic strength, disaggregation follows different paths in the three solutions and, since the titration stops at pH ≈ 10 , the disaggregation endpoint differs varying the total amount of exposed and titrated acidic groups. In conclusion, a combination of different disaggregation path, ionic strength, and surface charge, intimately interrelated with each other, can explain the

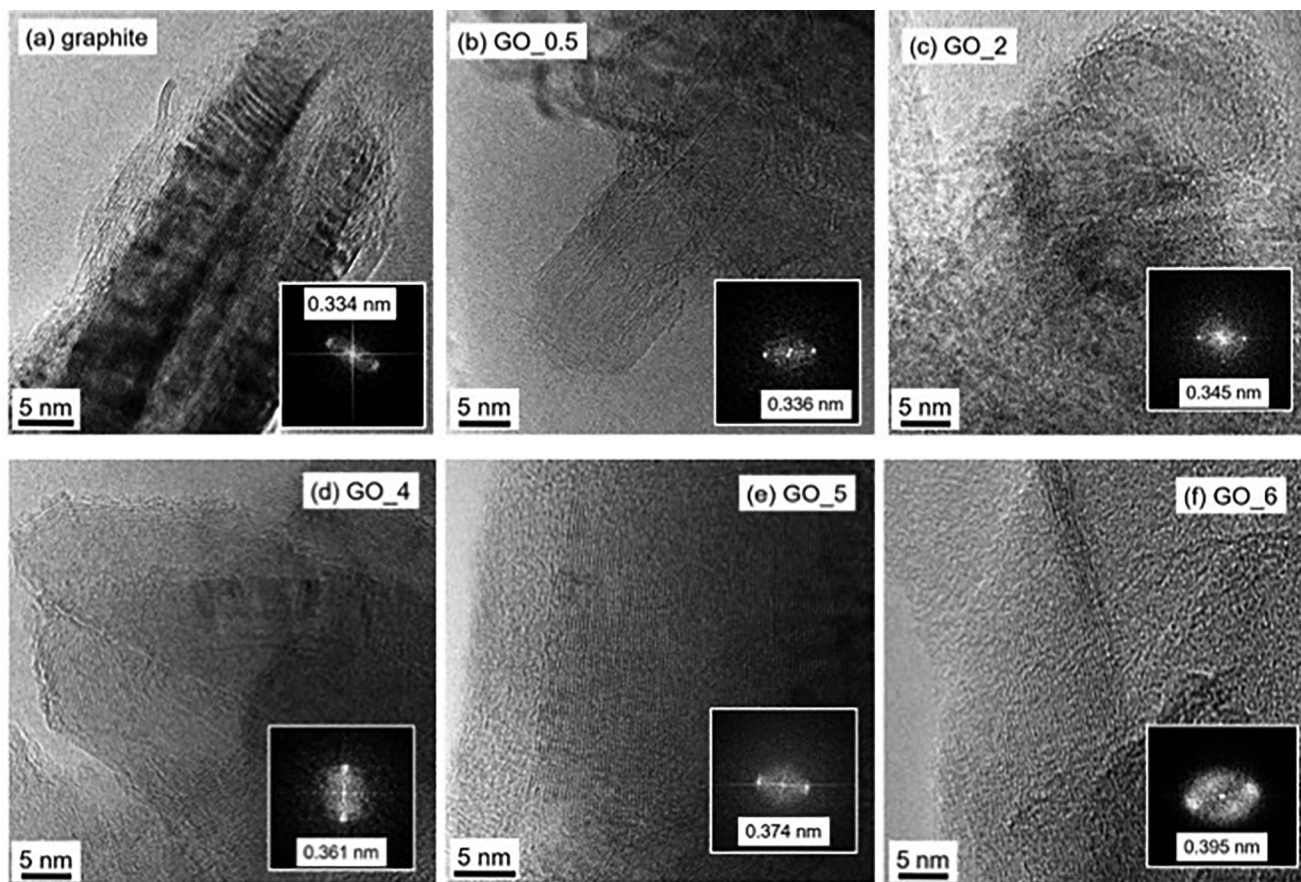


Figure 5. HRTEM images of a) pure graphite, b) GO_{0.5}, c) GO_{2.0}, d) GO_{4.0}, e) GO_{5.0}, and f) GO_{6.0} powders.

overestimation of carboxylic functionalities and it shows that Boehm titrations cannot be used to determine the amount of acidic functional groups on GO but, after elimination of oxidative debris, only on bwGO. Contrarily, the evaluation of basic functionalities is easier since, in acid solution, OD is stable on the graphene plane and it is not released. The determined amount corresponds to basic groups on the edge of graphene planes and eventually to basic groups on OD that protrude from bwGO. Table 1 shows the main outcomes: the basic moieties tend to decrease with the increase of the permanganate amount (down to $\approx 200 \mu\text{eq g}^{-1}$), corroborating the XPS results, until a plateau is reached from GO_{4.0} on.

As far as it concerns the morphology of both graphite and GO samples, HR-TEM analyses have been carried out to shed light on the changes induced by incipient oxidation during the preparation stage. Figure 5 resumes the situation evidenced by the inspection at high magnification for all the samples: it can be noted that peculiar fringe patterns are always evident and ascribable for the pure graphite sample to the (002) family plane in good agreement with the XRPD results reported above. The Fast Fourier Transform elaboration of the fringes (inset of Figure 5a) indicates that the distances are 0.334 nm, in agreement with those types of bare graphite (ICDD card n. 01-075-1621). Moreover, an increase in the distance (insets of Figure 5b–f) referred to the relevant fringes (up to $d = 0.395$ nm) is clearly appreciable by increasing the oxidation degree of the powders.

Regarding the surface properties of the as-synthesized GO, Brunauer–Emmett–Teller and Barrett–Joyner–Halenda (BET–BJH) analyses were carried out. As stated in Table 1 (third column), the specific surface area (S_{BET}) seems to slightly increase with the rise of the oxidation degree, passing from $11 \text{ m}^2 \text{ g}^{-1}$ of pristine graphite to $\approx 20 \text{ m}^2 \text{ g}^{-1}$. On the contrary, the total pores volume moderately reduces (from the reference value of $0.031 \text{ cm}^3 \text{ g}^{-1}$ of pure graphite; see Table 1, fourth column). The isotherm hysteresis exhibits an interesting behavior since it is clearly visible that, by increasing the oxidation degree, a considerable increase of the ultra-micropores (with diameter lower than $0.7 \text{ nm}^{[62]}$) occurs, as displayed in Figure S4 (Supporting Information), by the lack of hysteresis closure.

2.2. GO Adsorption Capacity as a Function of the Interlayer Distance

To correlate the different GO oxidation degrees and, subsequently, the possible different interlayer distances to a potential application in the field of environmental monitoring, adsorption kinetic tests were carried out. Specifically, taking into account that there is an effect of the molecule shape onto the degree of intercalation between the planes of GO,^[63] with a maximum for flat molecules, a planar pollutant molecule, for example, *o*-toluidine, was adopted. The adsorption performance was

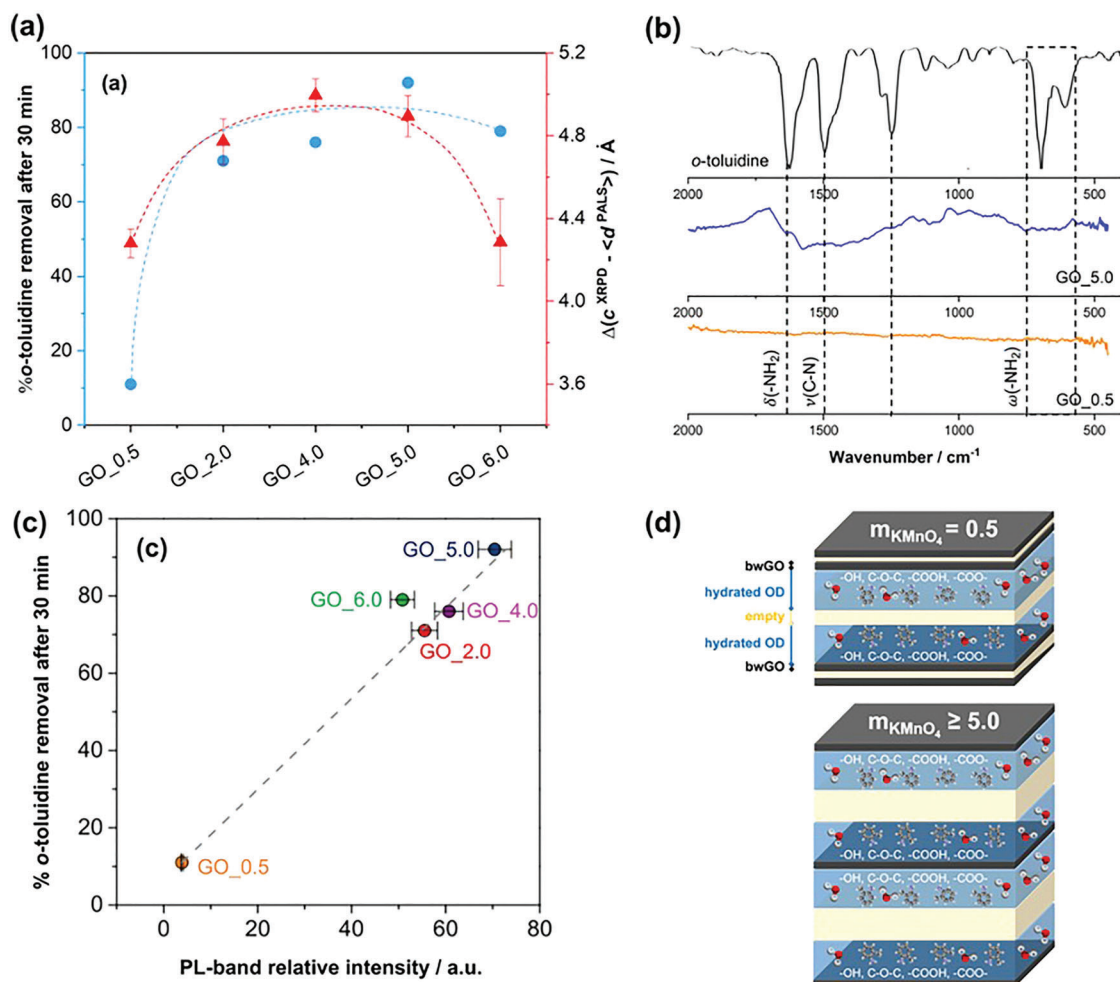


Figure 6. a) Percentage of aqueous *o*-toluidine removal (25 ppm starting concentration) after 30 min for GO_0.5, GO_2.0, GO_4.0, GO_5.0 and GO_6.0 (blue dots) compared to the difference between *c*-axis values by XRPD and the interlayer distance assessed by means of PALS technique ($\langle d^{PALS} \rangle$, red dots). Adsorption kinetics: pH 7, $c_{\text{GO}} = 0.67 \text{ mg L}^{-1}$, followed $\lambda = 280 \text{ nm}$. b) Comparison of FTIR spectra related to pure *o*-toluidine and subtraction between after 30 min and before the adsorption of the pollutant onto GO_0.5 and GO_5.0. c) Linear correlation between *o*-toluidine removal and relative intensity of the PL-band. d) Schematic representation of the sandwiched GO configuration in the case of GO_0.5 (left side) and GO_2.0, 4.0, 5.0, and 6.0 (right side) systems.

followed by means of UV/Vis spectroscopy (see Figure S5, Supporting Information^[44]), calculating the removal percentage both after only 30 min and 3 h. Being the pH of the solution near 7 and the total time of the kinetic study limited to 3 h, it is possible to consider negligible OD release and to assume that it does not affect the adsorption of *o*-toluidine. For all the GO powders, most of the pollutant adsorption occurred within half an hour (see inset of Figure S5, Supporting Information) and, in addition, the performance trend resembles the results obtained from the physicochemical characterizations (XRPD, micro-Raman, TGA, XPS, and Boehm titrations): an increase of the oxidation degree by increasing KMnO_4 followed by the achievement of a plateau at oxidant concentrations higher than 0.3 g (Figure 6a, blue dots). Also, in this case, GO_6.0 showed slightly worse behavior with respect to GO_5.0, reminding previous results (see 3.1 paragraph). In trying to better understand the *o*-toluidine intercalation into GO layers, Fourier-transform infrared (FTIR) analyses were also carried out. Figure 6b shows a comparison of spec-

tra obtained by subtracting those of pristine GO_0.5 or GO_5.0 from the corresponding ones recorded after the adsorption of *o*-toluidine (sampling at 30 min). Notably, only for the fully oxidized graphene (GO_5.0), new peaks related to the adsorbed pollutant appeared: at $\approx 1500\text{--}1270 \text{ cm}^{-1}$ those ascribable to the stretching of toluidine C–N bonds,^[64] while at 1620 and 700 cm^{-1} the scissoring/wagging of -NH_2 , respectively. As such, we confirmed once again a scarcer adsorption capability of GO_0.5 evidenced by an almost flat IR difference spectrum. According to the recent literature,^[65] aromatic phenyl amines prefer to be covalently bound to GO, through either nucleophilic reaction of the amine moiety with the graphene oxide basal plane or hydrogen bonding.^[66,67] As reported by Spyrou et al.,^[65] two mechanisms may be hypothesized to explain this interaction: the GO epoxy ring opening reaction or a nucleophilic reaction with the carbon of a hydroxyl group in α -position. A further corroboration of this amine-guided mechanism comes from other studies,^[65] which showed a weaker interaction occurring between GO and

the phenyl ring of the aromatic amines. Hence, we suppose that during *o*-toluidine intercalation into highly oxidized graphene (as GO_5.0), its molecules may assume a slightly tilted orientation, causing an impairment of the π - π stacking (as reported in^[65]) between the GO sheets, due to the high interaction among $-\text{NH}_2$ moieties and oxidized graphene species.

In order to match all these data up to the interlayer distance, the positron annihilation lifetime spectroscopy technique was used as already reported in a previous work by Panzarasa et al.^[3]. PALS is a suitable experimental technique to get information on the voids in non-metallic materials,^[68] where positronium (Ps), the electron-positron bound state, is localized. In a vacuum ortho-Ps (*o*-Ps) lifetime, the ground state with parallel spins of the two particles is 142 ns. The lifetime of para-Ps (*p*-Ps, anti-parallel spins) is 125 ps. In a void, *o*-Ps interacts with the electrons of the cavity and annihilation with an electron not belonging to Ps and in a relative singlet state is possible. Such a process (“pickoff” annihilation) reduces the *o*-Ps lifetime up to two orders of magnitude: the smaller the size of the void, the higher the probability of interaction between the positron and an external electron and the lower the *o*-Ps lifetime. This correlation is the core of PALS applications to materials characterized by voids (e.g., free volume holes in polymers), allowing an insight into the size of the void, provided that this void is approximated by a suitable geometry and applying a quantum-mechanical model that accounts for the annihilation of *o*-Ps in the cavity.

PALS spectra were analyzed in three discrete components. It is reasonable to relate the shortest lifetime component (≈ 200 ps) to positrons annihilating in the bulk as well as to *p*-Ps annihilations. Indeed, this last contribution cannot be resolved as a distinct component, due to the resolution of the apparatus and the faint intensity, expected to be of the order of one-third of the intensity of the longest one. The intermediate component (≈ 400 ps) is attributed to positrons annihilated into the cavities; the higher lifetime results from a lower electron density surrounding the positron with respect to the bulk. The longest component is due to the decay of *o*-Ps trapped in open volumes. The lifetimes of this last component (the only one of interest in the present paper) are displayed in Table S2 (Supporting Information).

o-Ps lifetime is generally translated into a typical size of the host cavity by using the Tao–Eldrup equation,^[69,70] which supplies, in spherical approximation, the corresponding radius *R*. However, in GO the voids are found in the interlayer distance; therefore, we used the following equation relying on the cavity hosting Ps as a parallelepiped as introduced by B. Jasinska et al.^[71] (for further details see the Supporting Information file). The relationship between *o*-Ps lifetime τ_3 , as determined experimentally, and the interlayer distance ($\langle d^{\text{PALS}} \rangle$) is:

$$\tau_3 = \frac{1}{\lambda_p} = \lambda_0^{-1} \left[1 - \left(\frac{d}{d + 2\Delta R} + \frac{1}{\pi} \sin \frac{\pi d}{d + 2\Delta R} \right) \right]^{-1} \quad (1)$$

where $\lambda_0 \approx 2 \text{ ns}^{-1}$ results from the spin-averaged annihilation rates of ortho and para-Ps, and ΔR ($= 0.166 \text{ nm}$) is an empirical parameter^[70,72] describing the penetration of the Ps wavefunction into the bulk. The values found for $\langle d^{\text{PALS}} \rangle$ are displayed in Table S2 (Supporting Information). Specifically, they represent the interlayer distance between (bwGO + OD) two-component layers of GO. However, since *o*-toluidine diffuses in an aque-

ous environment rather than in this “empty” interlayer, it would be better to compare the obtained adsorption percentages with the thickness of the hydrated OD grafted onto bwGO, which can be obtained by subtracting $\langle d^{\text{PALS}} \rangle$ from the interlayer distance measured by XRPD (c^{XRPD}). The obtained results are reported in Figure 6a. Notably, both the *o*-toluidine removal percentage and the computed difference trends are very similar exhibiting a sort of plateau curve. Moreover, as expected based on the above discussion, the *o*-toluidine adsorption values well correlate also with the relative intensity of the visible PL-band (by Raman analysis), which, similarly to $\langle d^{\text{PALS}} \rangle$, indirectly monitors the oxidation degree of GO (Figure 6c; $R^2 = 0.987$).

In conclusion, at low oxidation degrees (such as in GO_0.5) there are both unsplit and isolated graphene planes, conversely to what occurs at higher KMnO_4 content. In the latter case, the presence of a five-layer sandwiched configuration can be hypothesized: a bwGO graphene plane, a hydrated OD layer, an “empty” space, another hydrated OD, and, finally, a bwGO plane. The relative thickness of this structure strongly depends on the oxidation degree (see scheme in Figure 6d).

3. Conclusion

A deep analysis of the oxidation degree of graphene oxide was herein reported. Particularly, by increasing the amount of the permanganate oxidant from 0.5 to 6.0 g, we managed to tune the interlayer gap between GO sheets resulting in the achievement of a maximum value after 4.0 g before moving slightly down in the case of GO_6.0. Diffraction data together with micro-Raman outputs corroborate this observation: the Raman D-band significantly upshifts moving from sample GO_0.5 to GO_4.0, then it starts to decrease showing a trend very similar to that of the XRPD interlayer distance *c* (from 6.2 to ≈ 7.3 Å, and then down again to ≈ 7.1 Å). Moreover, by means of TGA measurements, a further assessment of the GO_0.5 similarity to pristine graphite was obtained, evidencing how this sample has structural interactions different from the other GO powders. In addition, once again, by increasing the GO oxidation degree, the temperature at which oxygen-containing groups are decomposed slightly decreases, reaching a sort of minimum for GO_4.0 and GO_5.0 and increasing again in GO_6.0. XPS and Boehm’s titrations shed new light on the surface properties of these GO materials. Particularly, the former confirmed the presence of differently oxidized surface groups and, above all, GO_5.0 and GO_6.0 seem to have a greater content of C *sp*³ to the detriment of C *sp*² bonds. As far as it concerns the Boehm titrations, instead, the achieved results led to hypothesize to be in presence of two different GO structures: a graphene with low oxidation degree showing functional groups decorating the edges of its plane (bwGO), and a second one composed of humic- and fulvic-like fragments known as oxidative debris, strongly adhering to graphene plane by means of π - π stackings and hydrogen bonds. The presence of these two components was further corroborated by HR-TEM images for all the GOs except for the less oxidized one, namely GO_0.5, in which OD is rarely present. A five-layer sandwiched configuration was hypothesized to represent the higher oxidation states (m_{KMnO_4} equal to or greater than 2.0). Finally, for the first time to the authors’ best knowledge, a correlation between the peculiar GO features and the materials’ adsorption capacity toward planar *o*-toluidine

molecules was drawn. The pollutant removal percentage with the variation of oxidant amount showed the same trend of the hydrated interlayer distance and Raman photoluminescence data, corroborating the fact that a too-high content of potassium permanganate (above 5.0) can be detrimental since the interlayer gap turns down (from 4.89 Å of GO_{5.0} and >90% of removal to 4.29 Å of GO_{6.0} and ≈80% of *o*-toluidine adsorption). Hence, we believe that the present findings can be useful for the development of GO-based intercalating materials in applications extending from membrane engineering to environmental monitoring.

4. Experimental Section

All the chemicals were of reagent-grade purity (by Sigma Aldrich) and were used without further purification; doubly distilled water passed through a Milli-Q apparatus was utilized.

Synthesis of GO Powders: Graphene Oxide was prepared by adopting a modified Hummers' method, already reported in the literature.^[35–37] Considering the effect of each parameter (temperature, relative humidity, concentration, and step duration) in the GO preparation,^[38,39] particular attention was paid to maintaining the same protocol in each synthesis. In a typical procedure, concentrated sulfuric acid (H₂SO₄, 96%, 50 cm³) was added to a mixture of graphite powder (1.0 g) and NaNO₃ (1.0 g). Then, the suspension was cooled down to 0 °C in an ice bath and a specific amount of KMnO₄ was slowly added to maintain the reaction temperature below 10 °C. Different graphene oxide powders were synthesized by varying the quantity of KMnO₄, namely 0.5, 2.0, 4.0, 5.0, and 6.0 g. The reaction mixture was stirred for 4 h and then, Milli-Q water (100 cm³) was slowly added keeping the solution in the ice bath. The suspension was stirred for a further 2 h at 70–80 °C. Subsequently, 200 cm³ of Milli-Q water at ≈60 °C was added, followed by an addition of 20 cm³ of hydrogen peroxide (H₂O₂, 30%v/v). Then, the reaction mixture was cooled down to room temperature and it was left to settle for a night. The resulting product was centrifuged and washed several times with Milli-Q water until a neutral pH was reached. In order to remove both the acidic traces and the salt residues, the powder was wrapped into a semi-permeable membrane for dialysis (Molecular Porous Membrane SpectraPor MWCO, 12–14 000). The washing step was monitored by measuring the conductivity of Milli-Q water until it reached a value lower than 5 μS cm⁻². Then, GO was dried in an oven at 60 °C (in the air).

GO powders were labeled as GO_{*x*}, where *x* is the amount of KMnO₄ used during the synthesis, that is, 0.5, 2.0, 4.0, 5.0, and 6.0 g.

XRPD patterns were obtained in Bragg–Brentano geometry at room temperature by Panalytical X'pert Pro high-resolution x-ray powder diffractometer equipped with a Cu tube (Cu-Kα_{1,2} radiation) and a thin nickel foil to suppress the Cu-Kβ radiation. The diffraction patterns were recorded in the 5° ≤ 2θ ≤ 55° range at a step size of 0.02° and a counting time of 15 s step⁻¹. The diffraction peaks were fitted with pseudo-Voigt functions using the program WinplotR^[40] to settle their 2θ positions, FWHM values, and integral intensities.

Raman scattering was measured in air by using an NTEGRA–Spectra SPM NT-MDT confocal microscope coupled to a solid-state laser operating at 2.33 eV (532 nm). The analysis was carried out by using a laser power of 250 μW (at the sample surface) to prevent local heating of the samples and annealing effects. The scattered light from the sample was collected by a 100× Mitutoyo objective, dispersed by 600 lines mm⁻¹ grating, and detected by a cooled ANDOR iDus CCD Camera. Further details on the instrumentation and data processing could be found elsewhere.^[41,42]

Thermogravimetric analyses were carried out by means of Mettler Toledo Star and System TGA/DSC 3+ under air atmosphere (5 °C min⁻¹ from 30 to 800 °C).

XPS data were collected with a Mprobe apparatus (Surface Science Instruments). The source was the monochromatic Al Kα radiation (1486.6 eV); a spot size of 200 × 750 nm and a pass energy of 25 eV were

used. The 1s level of hydrocarbon-contaminant carbon was taken as the internal reference at 284.6 eV. The accuracy of the reported binding energies (B.E.) could be estimated to be ≈0.2 eV and the resolution was equal to 0.74 eV.

The specific surface area (*S*_{BET}) and porosity distribution were obtained from N₂ adsorption/desorption isotherms at 77 K using a Tristar II 3020 (Micromeritics) apparatus and the instrumental software (Version 1.03) and applying BET–BJH analyses, respectively. Prior to measuring, sample powders were thermally pre-treated (*T* = 150 °C, 4 h, N₂) to remove adsorbed foreign species, for example, water.

The morphology was investigated by using HR–TEM. Analyses were performed on an HR-TEM JEOL 3010-UHR high-resolution transmission electron microscope (acceleration potential: 300 kV; LaB₆ filament). Samples were dry dispersed before the investigation on Cu grids covered with Lacey carbon without any further treatment.

In order to assess oxygen-containing functionalities on carbon materials, Boehm titrations were carried out.^[43] NaOH (0.05 M), Na₂CO₃ (0.05 M), NaHCO₃ (0.05 M), and HCl (0.05 M) solutions were prepared and standardized in triplicate. Then, four GO suspensions were prepared by adding 0.2 g of graphene oxide into 25 mL of each aqueous solution, and, for every powder, three titrations were carried out. The suspensions were left under stirring for 24 h and then centrifuged and filtered. In the case of alkaline solutions, a back titration was performed: three aliquots were taken from the filtrate of each sample and acidified using 0.05 M HCl for complete neutralization. For the acidic suspension, a direct titration of 5 mL of the filtrate was performed. All the acidified solutions were purged with N₂ under magnetic stirring for 15 min. Then, the aliquots were potentiometrically titrated with 0.05 M NaOH. Data were reported as average values together with the relative standard deviations.

FTIR spectra were acquired on a PerkinElmer Spectrum 100 spectrophotometer operating in attenuated total reflection mode equipped with a single-bounce diamond crystal with a 45° incidence angle. Spectra were recorded between 4000 and 400 cm⁻¹.

Concerning the positron annihilation lifetime spectroscopy, the positron source, a droplet of ²²Na (activity ≈10⁵ Bq) was deposited at the center of a Kapton foil (thickness 7.6 μm). Once dried, it was covered by an identical Kapton foil. The two foils were glued together, care that the glue did not contaminate the source. The source was placed between two layers of a GO sample in a “sandwich” configuration, contained in a plexiglass cylinder whose bases were made of filter paper to allow evacuation. The thickness of the GO sample was sufficient to stop all the injected positrons. The cylinder was inserted in a glass tube connected to a pumping system, able to guarantee a vacuum better than 10⁻⁴ mbar. Before starting the measurements, each sample was evacuated for 8 h. The glass tube was seen by two plastic (Pilot U) scintillators connected to a fast–fast coincidence setup; the resolution was 290 ps. Time annihilation spectra in triplicate for each sample were collected, each one having ≈1.5 × 10⁶ counts. They were analyzed by means of the computer code LT; a correction for the positrons annihilated in Kapton was considered.

To further corroborate the ability of GO sheets to entrap pollutant molecules, aqueous *o*-toluidine adsorption was evaluated accordingly. Kinetic tests were carried out at spontaneous pH (≈7), adopting a starting pollutant concentration of 25 ppm and GO concentration equal to 0.67 mg mL⁻¹. According to the previous study, direct photolysis of *o*-toluidine could be considered negligible,^[44] therefore the kinetics were performed under ambient light conditions. In order to assess the GO adsorption capacity, UV/Vis spectra were acquired after samplings filtration (MF-Millipore Membrane Filter, 0.45 μm pore size) at 30, 60, 90 and 180 min, by following the maximum wavelength at 280 nm.

Supporting Information

Supporting Information is available from the Wiley Online Library or from the author.

Acknowledgements

The authors gratefully acknowledge Dr. Ottavio Lugaresi and Prof. Daniela Maggioni for the TGA and FTIR analyses, respectively. M.L. and G.C. acknowledge partial funding by National Recovery and Resilience Plan (NRRP), Mission 4 Component 2 Investment 1.3 – Call for tender No. 1561 of 11.10.2022 of Ministero dell'Università e della Ricerca (MUR); funded by the European Union – NextGenerationEU. Award Number: Project code PE0000021, Concession Decree No. 1561 of 11.10.2022 adopted by Ministero dell'Università e della Ricerca (MUR), CUP D43C22003090001, Project title "Network 4 Energy Sustainable Transition – NEST".

Conflict of Interest

The authors declare no conflict of interest.

Author Contributions

Conceptualization was done by M. L. and G.C.; Formal analysis was done by E.P., G.C., S.S., M.L., S.P., P.C., and M.S.; Investigation was done by all authors; Supervision was done by M.L. and G.C.; E.P., G.C., S.S., P.C., and M.S. wrote the original draft; M.L. and G.C. wrote, reviewed and edited.

Data Availability Statement

The data that support the findings of this study are available from the corresponding author upon reasonable request.

Keywords

exfoliation, graphene oxides, *o*-toluidine adsorption, oxidation degrees, positron annihilation lifetime spectroscopy technique

Received: March 3, 2023

Revised: May 12, 2023

Published online:

- [1] P. Johari, V. B. Shenoy, *ACS Nano* **2011**, *5*, 7640.
- [2] W. Zhan, Z. Xu, X. Yang, *Sep. Purif. Technol.* **2020**, *233*, 116029.
- [3] G. Panzarasa, G. Consolati, M. Scavini, M. Longhi, F. Quasso, *C* **2019**, *5*, 6.
- [4] J. Kwon, B. Lee, *Chem. Eng. Res. Des.* **2015**, *104*, 519.
- [5] L. Tang, X. Li, R. Ji, K. S. Teng, G. Tai, J. Ye, C. Wei, S. P. Lau, *J. Mater. Chem.* **2012**, *22*, 5676.
- [6] C. H. Chen, S. Hu, J. F. Shih, C. Y. Yang, Y. W. Luo, R. H. Jhang, C. M. Chiang, Y. J. Hung, *Sci. Rep.* **2017**, *7*, 3908.
- [7] T. T. Wu, J. M. Ting, *Surf. Coat. Technol.* **2013**, *231*, 487.
- [8] S. Zhang, Z. Zhang, W. Yang, *Appl. Surf. Sci.* **2016**, *360*, 323.
- [9] X. Jiang, J. Nisar, B. Pathak, J. Zhao, R. Ahuja, *J. Catal.* **2013**, *299*, 204.
- [10] S. Thangavel, G. Venugopal, *Powder Technol.* **2014**, *257*, 141.
- [11] R. Maiti, A. Midya, C. Narayana, S. K. Ray, *Nanotechnology* **2014**, *25*, 495704.
- [12] C.-H. Chen, S. Hu, J.-F. Shih, C.-Y. Yang, Y.-W. Luo, R.-H. Jhang, C.-M. Chiang, Y.-J. Hung, *Sci. Rep.* **2017**, *7*, 3908.
- [13] F. Ai, Y. Zhong, X. Hu, X. Yan, *J. Wuhan Univ. Technol., Mater. Sci. Ed.* **2016**, *31*, 515.
- [14] K. A. Mkhoyan, A. W. Contryman, J. Silcox, D. A. Stewart, G. Eda, C. Mattevi, S. Miller, M. Chhowalla, *Nano Lett.* **2009**, *9*, 1058.
- [15] T. Szabó, E. Tombácz, E. Illés, I. Dékány, *Carbon* **2006**, *44*, 537.
- [16] R. B. Chilakapati, S. Hemanth Kumar, S. V. Satyanarayana, D. K. Behara, *Z. Phys. Chem.* **2021**, *235*, 1645.
- [17] L. Xu, H. Suo, R. Liu, H. Liu, H. Qiu, *RSC Adv.* **2019**, *9*, 30125.
- [18] H. Zhu, T. Chen, J. Liu, D. Li, *RSC Adv.* **2018**, *8*, 2616.
- [19] A. Colombo, G. Cappelletti, S. Ardizzone, I. Biraghi, C. L. Bianchi, D. Meroni, C. Pirola, F. Spadavecchia, *Environ. Chem. Lett.* **2012**, *10*, 55.
- [20] X. Xue, J. Xu, S. A. Baig, X. Xu, *J. Taiwan Inst. Chem. Eng.* **2016**, *59*, 365.
- [21] Y. Zhang, M. Dai, K. Liu, C. Peng, Y. Du, Q. Chang, I. Ali, I. Naz, D. P. Saroj, *RSC Adv.* **2019**, *9*, 30240.
- [22] N. S. Tabrizi, S. Zamani, *Water Sci. Technol.* **2016**, *74*, 256.
- [23] J. Xu, Y. F. Zhu, *Acta Phys.-Chim. Sin.* **2013**, *29*, 829.
- [24] T. Phatthanakittiphong, G. T. Seo, *Nanomaterials* **2016**, *6*, 128.
- [25] W. Xu, Y. Chen, W. Zhang, B. Li, *Adv. Powder Technol.* **2019**, *30*, 493.
- [26] M. Abbaz, Y. Azougarh, M. Benafqir, Z. Anfar, N. El Alem, *Mediterr. J. Chem.* **2018**, *7*, 1.
- [27] B. Rezania, N. Severin, A. V. Talyzin, J. P. Rabe, *Nano Lett.* **2014**, *14*, 3993.
- [28] Y. L. Xing, G. R. Xu, Z. H. An, Y. H. Liu, K. Xu, Q. Liu, H. L. Zhao, R. Das, *Sep. Purif. Technol.* **2021**, *259*, 118192.
- [29] L. Liu, R. Zhang, Y. Liu, H. Zhu, W. Tan, G. Zhu, Y. Wang, *Trans. Tianjin Univ.* **2018**, *24*, 555.
- [30] S. Liang, S. Wang, L. Chen, H. Fang, *Sep. Purif. Technol.* **2020**, *241*, 116738.
- [31] J. Guerrero-Contreras, F. Caballero-Briones, *Mater. Chem. Phys.* **2015**, *153*, 209.
- [32] K. Krishnamoorthy, M. Veerapandian, K. Yun, S. J. Kim, *Carbon* **2013**, *53*, 38.
- [33] S. Mostoni, V. Pifferi, L. Falciola, D. Meroni, E. Pargoletti, E. Davoli, G. Cappelletti, *J. Photochem. Photobiol., A* **2017**, *332*, 534.
- [34] V. Pifferi, G. Cappelletti, S. Ardizzone, L. Falciola, C. Di Bari, F. Spadavecchia, D. Meroni, A. Carrà, G. Cerrato, S. Morandi, E. Davoli, *Appl. Catal., B* **2015**, *178*, 233.
- [35] J. Chen, B. Yao, C. Li, G. Shi, *Carbon* **2013**, *64*, 225.
- [36] E. Pargoletti, U. H. Hossain, I. Di Bernardo, H. Chen, T. Tran-Phu, J. Lipton-Duffin, G. Cappelletti, A. Tricoli, *Nanoscale* **2019**, *11*, 22932.
- [37] E. Pargoletti, U. H. Hossain, I. Di Bernardo, H. Chen, T. Tran-Phu, G. L. Chiarello, J. Lipton-Duffin, V. Pifferi, A. Tricoli, G. Cappelletti, *ACS Appl. Mater. Interfaces* **2020**, *12*, 39549.
- [38] C. Mora, A. Buljan, T. Figueroa, *ACS Appl. Nano Mater.* **2022**, *5*, 4648.
- [39] A. Lurf, A. Buchsteiner, J. Pieper, S. Schöttl, I. Dekany, T. Szabo, H. P. Boehm, *J. Phys. Chem. Solids* **2006**, *67*, 1106.
- [40] T. Roisnel, J. Rodríguez-Carvajal, *Mater. Sci. Forum* **2001**, *378–381*, 118.
- [41] Y. Belaustegui, S. Zorita, F. Fernández-Carretero, A. García-Luis, F. Pantò, S. Stelitano, P. Frontera, P. Antonucci, S. Santangelo, *Desalination* **2018**, *428*, 40.
- [42] B. Ma, R. D. Rodriguez, A. Ruban, S. Pavlov, E. Sheremet, *Phys. Chem. Chem. Phys.* **2019**, *21*, 10125.
- [43] H. P. Boehm, *Adv. Catal.* **1966**, *16*, 179.
- [44] G. Cappelletti, V. Pifferi, S. Mostoni, L. Falciola, C. Di Bari, F. Spadavecchia, D. Meroni, E. Davoli, S. Ardizzone, *Chem. Commun.* **2015**, *51*, 10459.
- [45] A. C. Ferrari, J. Robertson, *Phys. Rev. B* **2000**, *61*, 14095.
- [46] L. G. Cançado, K. Takai, T. Enoki, M. Endo, Y. A. Kim, H. Mizusaki, N. L. Speziali, A. Jorio, M. A. Pimenta, *Carbon* **2008**, *46*, 272.
- [47] C. Greco, U. Cosentino, D. Pitea, G. Moro, S. Santangelo, S. Patanè, M. D'Arienzo, M. Fiore, F. Morazzoni, R. Ruffo, *Phys. Chem. Chem. Phys.* **2019**, *21*, 6021.
- [48] S. Santangelo, G. Messina, G. Faggio, S. H. Abdul Rahim, C. Milone, *J. Raman Spectrosc.* **2012**, *43*, 1432.
- [49] T.-F. Yeh, J.-M. Syu, C. Cheng, T.-H. Chang, H. Teng, *Adv. Funct. Mater.* **2010**, *20*, 2255.

- [50] S. Santangelo, M. Lanza, C. Milone, *J. Phys. Chem.* **2013**, *117*, 4815.
- [51] C. T. Chien, S. S. Li, W. J. Lai, Y. C. Yeh, H. A. Chen, I. S. Chen, L. C. Chen, K. H. Chen, T. Nemoto, S. Isoda, M. Chen, T. Fujita, G. Eda, H. Yamaguchi, M. Chhowalla, C.-W. Chen, *Angew. Chem., Int. Ed.* **2012**, *51*, 6662.
- [52] E. T. Mombeshora, P. G. Ndungu, V. O. Nyamori, *New Carbon Mater.* **2017**, *32*, 174.
- [53] X. Cai, Q. Zhang, S. Wang, J. Peng, Y. Zhang, H. Ma, J. Li, M. Zhai, *J. Mater. Sci.* **2014**, *49*, 5667.
- [54] S. Muralikrishna, K. Sureshkumar, T. S. Varley, D. H. Nagaraju, T. Ramakrishnappa, *Anal Methods* **2014**, *6*, 8698.
- [55] M. C. Hsiao, C. C. M. Ma, J. C. Chiang, K. K. Ho, T. Y. Chou, X. Xie, C. H. Tsai, L. H. Chang, C. K. Hsieh, *Nanoscale* **2013**, *5*, 5863.
- [56] E. Pargoletti, S. Verga, G. L. Chiarello, M. Longhi, G. Cerrato, A. Giordana, G. Cappelletti, *Nanomaterials* **2020**, *10*, 761.
- [57] D. W. Lee, J. W. Seo, *J. Phys. Chem.* **2011**, *115*, 2705.
- [58] A. Naumov, F. Grote, M. Overgaard, A. Roth, C. E. Halbig, K. Nørgaard, D. M. Guldi, S. Eigler, *J. Am. Chem. Soc.* **2016**, *138*, 11445.
- [59] J. P. Rourke, P. A. Pandey, J. J. Moore, M. Bates, I. A. Kinloch, R. J. Young, N. R. Wilson, *Angew. Chem., Int. Ed.* **2011**, *50*, 3173.
- [60] I. Martin-Gullon, J. M. Pérez, D. Domene, A. J. A. Salgado-Casanova, L. R. Radovic, *Carbon* **2020**, *158*, 406.
- [61] J. Zhang, C. Xiong, Y. Li, H. Tang, X. Meng, W. Zhu, *J. Hazard. Mater.* **2021**, *402*, 123552.
- [62] T. J. Bandoz, M. J. Biggs, K. E. Mark, Y. Gubbins, T. Hattori, K. Iiyama, J. Kaneko, J. Pinunik, K. T. Thomson, L. R. Radovic, *Molecular models of porous carbons*, in: Chem. Phys. Carbon, Marcel Dekker Inc., Basel, **2003**, p. 118.
- [63] A. Nordenström, N. Boulanger, A. Iakunkov, I. Baburin, A. Klechikov, A. Vorobiev, A. V. Talyzin, *J. Phys. Chem.* **2021**, *125*, 6877.
- [64] S. Dacrory, E. S. A. Haggag, A. M. Masoud, S. M. Abdo, A. A. Eliwa, S. Kamel, *Cellulose* **2020**, *27*, 7093.
- [65] K. Spyrou, M. Calvaresi, E. K. Diamanti, T. Tsoufis, D. Gournis, P. Rudolf, F. Zerbetto, *Adv. Funct. Mater.* **2015**, *25*, 263.
- [66] C. Sun, Y. Deng, L. Wan, X. Qin, G. Chen, *ACS Appl. Mater. Interfaces* **2014**, *6*, 11277.
- [67] S. K. Jha, M. Roth, G. Todde, J. P. Buchanan, R. D. Moser, M. K. Shukla, G. Subramanian, *J. Phys. Chem.* **2018**, *122*, 1288.
- [68] Y. C. Jean, J. D. Van Horn, W. S. Hung, K. R. Lee, *Macromolecules* **2013**, *46*, 7133.
- [69] S. J. Tao, *J. Chem. Phys.* **1972**, *56*, 5499.
- [70] M. Eldrup, D. Lightbody, J. N. Sherwood, *Chem. Phys.* **1981**, *63*, 51.
- [71] B. Jasińska, A. E. Koziół, T. Goworek, *Acta Phys. Pol., A* **1999**, *95*, 557.
- [72] H. Nakanishi, J. Wang, *Positron Annihilation Studies of Fluids*, World Scientific, Singapore **1988**.